Construction of a Total Internal Reflection Fluorescence Microscope to Study Lipid Domain Composition via Raman Spectral Imaging

Submitted to the Pomona College Physics Department in Partial Fulfillment of the Bachelor of Arts Degree in Physics

Kevin Kelley
Pomona College

Advisor: Alfred Kwok
May 2009

Table of Contents

1 Abstract

The plasma membrane is not homogeneous and contains domains, which are enriched in cholesterol and sphingolipid, implicated in numerous biological pathways. In order to quantitatively study the composition of lipid domains via Raman spectroscopy we constructed a total internal reflection fluorescence (TIRF) microscope. We have successfully obtained TIR-fluorescence spectra from a phosphatidylcholine bilayer containing 2% mole fraction of phosphatidylethanolamine with fluorescent head groups. The development of the TIRF microscope, which will provide the framework for future TIR Raman experiments of lipid domains, is described in this study.

2 Introduction

2.1 The Lipid Raft Hypothesis

Cell membranes define the limiting boundary of eukaryotic cells, actively restricting access to the cellular interior by the external environment, and playing an important role in the exchange of nutrients and metabolites (Sengupta *et al.* 2007). The fluid mosaic model (Singer & Nicholson 1972) has been the standard textbook description of cell membranes for the past 30 years: lipids and proteins which make up the membrane are free to move laterally throughout the membrane to form a homogenous fluid lipid bilayer. However, biophysicists find that lipids exist in several phases in model bilayers, including gel, liquid-ordered and liquid-disordered (Simons & Toomre 2001). In the gel state lipids are solid-like; in the liquid-disordered state the entire bilayer is fluid, as proposed by the Singer-Nicholson model. In the liquid-ordered phase, phospholipids with saturated hydrocarbon chains pack tightly with cholesterol, but remain mobile in the plane of the membrane (Simons & Toomre 2001). The complex nature of the cell has made it difficult to show that lipids exist in these different phases.

The lipid raft hypothesis (Simons & Ikonen 1997), originating from studies on epithelial cell polarity, is based on the concept that lipids in the plasma membrane have different biophysical propensities to associate with each other and proposes the existence of lipid domains as a result of these interactions. Lipid domains consist of dynamic assemblies of cholesterol and saturated and mono-unsaturated phospholipids (or sphingolipids) that form moving platforms, or "rafts" onto which specific proteins attach. Since then, immunofluorescence transmission electron microscopy and single molecule tracking have been used to provide evidence for ~50-200 nm lipid-protein membrane

domains in biological systems such as Prion proteins and neurons (Brugger *et. al*. 2004). The raft hypothesis associates functional significance with lipid domains and proposes their active role in numerous signal transduction pathways, apoptosis, and exocytosis and endocytosis functions (Simons & Toomre 2001, Michel & Bakovic 2007). Lipid raft involvement has also been suggested to take place in a variety of diseases, such as Alzheimer's disease and HIV (Cordy *et. al.* 2006, Rejendran & Simons 2005). An understanding of the physical properties (i.e. line tensions, critical fluctuations, and composition) of lipid rafts thus has the potential to increase our understanding of cell signaling and the potential to solve many important health related problems

2.2 Phase Separation in Model Membranes

Studying lipid rafts in living cells is challenging. Biological membranes are complex structures that contain a large amount of proteins. Moreover, lipid rafts are too small to be observed by light microscopy (Simons & Toomre 2001). By using model membranes, we can study how specific membrane components interact by only incorporating these specific components into the membrane. Therefore, model membranes have historically been used to study membrane domains and these studies have provided a significant contribution to the study of lipid rafts.

In the past seven years, fluorescence microscopy has been used to directly visualize micron-sized lipid domains in model membranes in the form of giant unilamellar vesicles (Veatch & Keller 2002, Veatch & Keller 2003) and planar supported bilayers (Dietrich *et. al.* 2001) consisting of ternary lipid mixtures with a wide range of compositions and temperatures. Probes with fluorophores attached to lipid head groups such as Texas Red – dipalmitoyl-phosphatidylethanolamine (Texas Red is the common

name for sulforhodamine 101 acid chloride, a red fluorescent dye) are used because they are preferentially included or excluded from the micron-sized liquid-ordered domains (see insets 4-8 in Figure 1). Liquid-ordered domains are found to exist for a long list of ternary mixtures of high melting temperature (saturated) lipid, low melting temperature (unsaturated) lipids and cholesterol (Veatch & Keller 2003). For the model mixture, dipalmitoylphosphatidylcholine/dioeleoylphosphatidylcholine/cholesterol (DPPC/DOPC/Chol) two coexisting liquid phases are observed over a wide range of lipid composition and temperature. Because of its similar saturated structure, DPPC can be used instead of SM to create lipid domains. It has been proposed that one of the phases is rich in unsaturated lipid and the other is rich in the saturated lipid and cholesterol. The mapped phase boundary for the full ternary system is shown in Figure 1. The phase diagram (Figure 1) contains several regions with varying compositions. One observes the existence of a liquid-liquid coexistence region where one of the phases is the liquid-disordered phase that is rich in DOPC while the other is the liquid-ordered phase (grey region) that is rich in DPPC and cholesterol.

However, as one sees from the figure, the lack of complete composition information of each phase prevents quantitative phase boundaries from being drawn (the figure is more of a sketch). But, as Veatch & Keller state, "clear, quantitative comparisons between different methods are needed, particularly since so many operational definitions and length-scales for 'rafts' are currently used" (Veatch & Keller 2003). Currently, there is no method which provides a quantitative means of determining the composition of lipid domains. Such a method would provide researchers with a means to quantitatively compare their membrane systems.

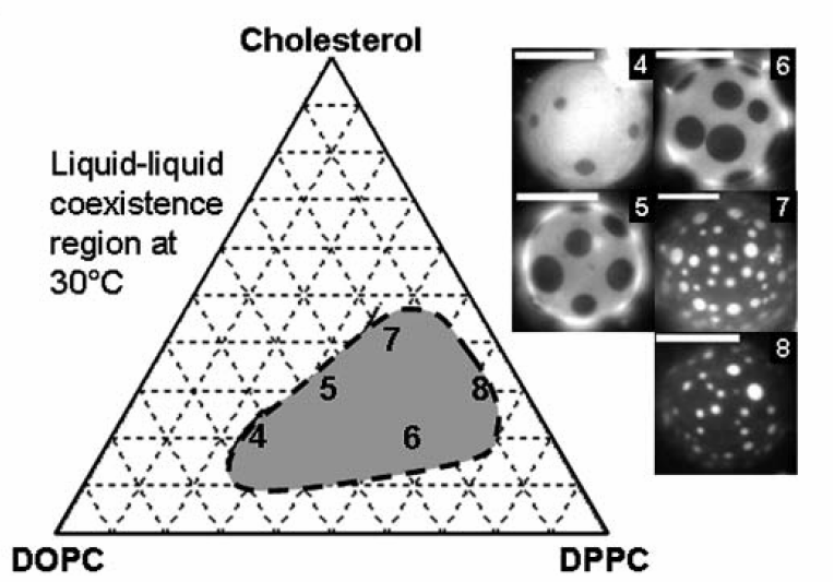

Figure 1: Observed phase diagram of micron-scale liquid immiscibility region in giant unilamellar vesicles. Compositions of vesicles in micrographs 4-8 are in order of increasing saturated lipid (DPPC) with Texas Red-DPPE (which is preferentially excluded from lipid domains). Above a certain concentration of DPPC (between micrographs 5 and 7) the dark and light regions flip because DPPC is now the predominant lipid in the sample (Veatch & Keller 2003).

2.3 Total Internal Reflection Fluorescence

The total internal reflection fluorescence (TIRF) microscope, developed in this study, will be the framework for many important Raman imaging experiments. These experiments will be able to quantitatively measure the composition of lipid microdomains in supported bilayers and could provide answers to important questions concerning membrane composition and function. We will use total internal reflection Raman to determine how much sphingomyelin and cholesterol are incorporated into liquid-ordered domains in supported bilayers. Supported bilayers can be analyzed by surface specific techniques and allow for the creation of model asymmetric bilayers (Kiessling *et. al.* 2006). Studying the composition inside and outside of liquid-ordered domains and the

spatial distribution of sphingomyelin and cholesterol will allow us to understand how the formations of liquid-ordered domains are related to various models in the literature.

To maximize the signal to noise ratio in our spectra, we have chosen to use prism-based total internal reflection to excite Raman scattering from our supported bilayer. In order for this setup to be successful, it is first necessary to construct a TIRF microscope to ensure that total internal reflection is indeed happening. TIRF microscopy provides a means to selectively excite fluorophores in an aqueous environment very near a solid surface (within < 100 nm) without exciting fluorescence in regions farther from the surface (Axelrod 2003). Fluorescence excitation by this thin zone of electromagnetic energy results in images with very low background fluorescence, and virtually no out of focus fluorescence. This thin layer of illumination is an "evanescent field" produced by an excitation light beam in solid (e.g. the prism and coverslip) that is incident at a high angle upon the solid-liquid surface at which the supported bilayer adheres. The incidence angle, measured from the normal, must be greater than the "critical angle" (defined by the indices of refraction of the solid and liquid) for the beam to totally reflect rather than refract through the surface.

The unique features of TIRF have enabled numerous applications in biochemistry and cell biology. TIRF has been used to selectively visualize cell/substrate contact regions (Weiss *et. al* 1982), to visualize and analyze single molecule fluorescence near a surface (Khan *et. al* 2000), to track secretory granules in intact cells (Steyer & Almers 1999), to measure the kinetic rates of binding of extracellular and intracellular proteins (Sund & Axelrod 2000), and to acquire long-term fluorescence movies of cells during development (Wang & Axelrod 1994).

Ultimately the evanescent field created by total internal reflection will be used to excite Raman scattering from our supported bilayer. Raman scattering is a species-specific technique that enables the characterization of the molecular species in a sample. Monochromatic light illuminates a sample, and the wavelength of the Raman-scattered light is longer than that of the incident laser because of energy loss to the vibrational modes of the molecules in the sample. The scattered light can then be spectrally dispersed to obtain the Raman spectrum of the sample, which contains a series of peaks at frequencies that correspond to the vibrational modes of the molecular species in the sample. Low signal to noise ratios is a problem for Raman spectroscopy due to the fact that a very small proportion of scattered photons make up the Raman signal. In physiological conditions (i.e. supported bilayers or vesicles) lipid Raman signals are dominated by the signal from the surrounding solution. For example, in a supported bilayer sample there are approximately 10^4 water molecules contributing to the spectrum for each lipid molecule (Lee *et al.* 2005). Even though the Raman scattering cross-section of water is weak relative to the lipid, the water is in vast excess and will swamp out the lipid signal.

We use prism-based total internal reflection, in which a prism is placed on top of the sample chamber which in turn is placed on top of an inverted microscope (see Figure 2). Prism-based total internal reflection will substantially reduce background Raman scattering from the water, since only material within the evanescent field contributes to the Raman spectrum. Raman scattering from the water will be significantly reduced because this region is farther from the interface.

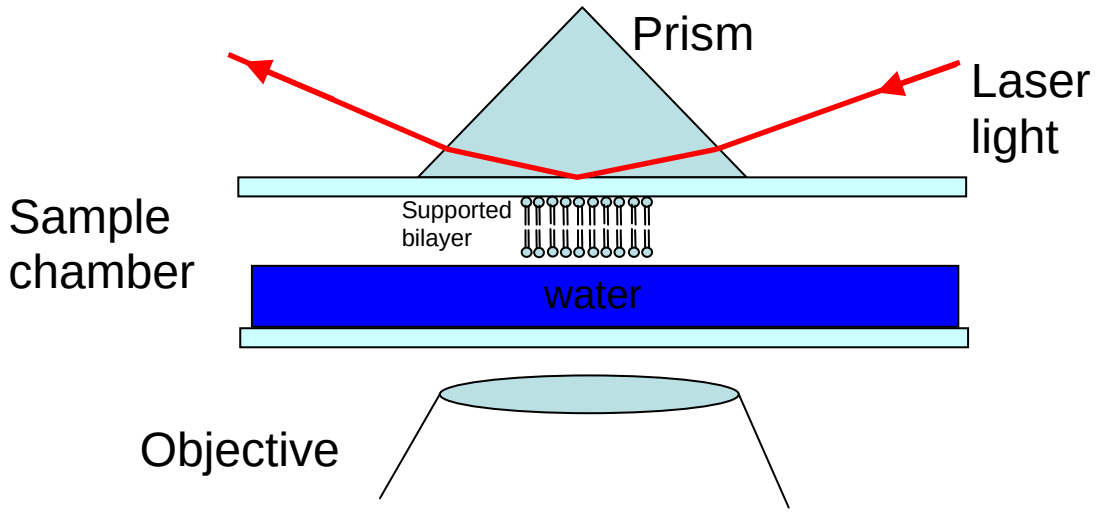

Figure 2: Diagram of the prism-based total internal reflection setup. Not drawn to scale.

Total internal reflection Raman scattering has been successfully used to obtain high quality vibrational spectra of planar supported lipid bilayers at the silica/water interface without the use of resonance or surface enhancement (Lee & Bain 2005). In their study spectra are reported of the phospholipids DMPC, DPPC, and POPC, in the C-H stretching region and the "fingerprint" region (1500-1900 cm^{-1}). We hope to build on this article by analyzing the Raman spectrums of phospholipids in order to obtain quantitative information.

The TIRF microscope setup constructed here will be the platform for years of future research using total internal reflectance Raman excitation. These experiments will verify that lipid domains distinguished by fluorescence are enriched in cholesterol and sphingomyelin and establish that Raman imaging is a viable and important technique for understanding the physical properties of lipids in supported bilayers.

3 Theory

3.1 Wave Equation and Solutions

The propagation of waves in one dimension can be described by the wave equation:

$$\frac{\partial^2 f}{\partial z^2} = \frac{1}{v^2}\frac{\partial^2 f}{\partial t^2} \tag{1}$$

where f is the displacement of the wave as a function of position z and time t, and v is the speed of the wave. All the solutions to equation (1) are functions, g, of the form:

$$f(z,t) = g(z \pm vt). \tag{2}$$

Such functions represent waves propagating in the z direction with speed v. Of all possible solutions, the sinusoidal is the most familiar:

$$f(z,t) = A\cos[k(z - vt) + \delta] \tag{3}$$

$$= A\cos[kz - \omega t + \delta] \tag{4}$$

$$= \mathrm{Re}\left[Ae^{i(kz-\omega t+\delta)}\right] \tag{5}$$

where A is the amplitude of the wave and δ is the phase constant. k is the wave number and is related to the wavelength and angular frequency, ω, by the relation, $\omega = kv$. We can rewrite equation (5) as:

$$\tilde{f}(z,t) \equiv \tilde{A}e^{i(kz-\omega t)} \tag{6}$$

with the complex amplitude $\tilde{A} \equiv Ae^{i\delta}$ absorbing the phase constant.

The natural generalization to three dimensions of equation (1) is given by:

$$\nabla^2 f = \frac{1}{v^2}\frac{\partial^2 f}{\partial t^2} \tag{7}$$

where ∇ is the del operator. In electromagnetic waves the displacement function, *f*, is a vector which represents the electric field, **E**, or the magnetic field, **B**. Boldface or arrows on top of the letter indicate vectors.

3.2 Electromagnetic Waves

3.2.1 Electromagnetic Waves in Vacuum

In a vacuum, there is no charge or current and therefore Maxwell's equations can be written as:

$$\begin{aligned} &\text{(i)}\ \ \vec{\nabla}\cdot\vec{E}=0 \quad \text{(iii)}\ \ \vec{\nabla}\times\vec{E}=-\frac{\partial\vec{B}}{\partial t} \\ &\text{(ii)}\ \ \vec{\nabla}\cdot\vec{B}=0 \quad \text{(iv)}\ \ \vec{\nabla}\times\vec{B}=\mu_0\varepsilon_0\frac{\partial\vec{E}}{\partial t}. \end{aligned} \tag{8}$$

It can be shown (Appendix I) that, when decoupled, each Cartesian component of **E** and **B** satisfies the three dimensional wave equation, equation (7):

$$\nabla^2\vec{E}=\mu_0\varepsilon_0\frac{\partial^2\vec{E}}{\partial t^2} \tag{9}$$

$$\nabla^2\vec{B}=\mu_0\varepsilon_0\frac{\partial^2\vec{B}}{\partial t^2} \tag{10}$$

where μ_0 is the permeability of free space and ε_0 is the permittivity of free space. Maxwell's equations imply that empty space supports the propagation of electromagnetic waves, traveling at a speed:

$$v=\frac{1}{\sqrt{\varepsilon_0\mu_0}}=3.00\times10^8\ \text{m/s}, \tag{11}$$

the velocity of light, *c*.

3.2.2 Monochromatic Plane Waves

The fields are uniform over every plane perpendicular to the direction of propagation in a plane electromagnetic wave. We limit the majority of our theoretical discussion to plane waves because they are mathematically simple. Moreover, any wave can be approximated as a plane wave, as long as its wavelength is much less than the radius of curvature of the wave front. Electromagnetic plane waves in 3-Dimensions can be described by:

$$\tilde{\vec{E}}(\vec{r},t) = \tilde{E}_0 e^{i\left(\vec{k}\cdot\vec{r}-\omega t\right)}\hat{n} \tag{12}$$

$$\tilde{\vec{B}}(\vec{r},t) = \tilde{B}_0 e^{i\left(\vec{k}\cdot\vec{r}-\omega t\right)}\left(\hat{k}\times\hat{n}\right) = \frac{1}{c}\hat{k}\times\tilde{\vec{E}} \tag{13}$$

where $\vec{n}$ is the direction of the electric field.

3.2.3 Energy in Electromagnetic Waves

The energy flux density (i.e. energy per unit area) per unit time transported by electromagnetic waves is given by the Poynting vector:

$$\vec{S} = \frac{1}{\mu_0}\left(\vec{E}\times\vec{B}\right). \tag{14}$$

Equation (14) can be rewritten as (see Appendix II):

$$\tilde{\vec{S}} = \frac{1}{c\mu_0}\left(\tilde{\vec{E}}\cdot\tilde{\vec{E}}^{*}\right)\hat{k} \tag{15}$$

$$\Rightarrow S = \left|\tilde{\vec{S}}\right| = \frac{1}{c\mu_0}\tilde{\vec{E}}\cdot\tilde{\vec{E}}^{*}. \tag{16}$$

Because light has a short period, most measurements will involve many cycles. Therefore, we are more interested in the average of the amplitude of the Poynting vector:

$$\langle S\rangle = \frac{1}{c\mu_0}\left\langle\tilde{\vec{E}}\cdot\tilde{\vec{E}}^{*}\right\rangle = \frac{1}{c\mu_0}\tilde{\vec{E}}\cdot\tilde{\vec{E}}^{*} \tag{17}$$

where the brackets denote the time average over a complete cycle. Since the dot product gets rid of time dependence the brackets can be dropped. The intensity of an electromagnetic wave is defined as the average power per unit area transported by an electromagnetic wave. For convenience, dropping the constants in equation (17), we can say that the intensity, *I*, is represented as the squared amplitude of the complex electric field vector:

$$I = \tilde{\vec{E}} \cdot \tilde{\vec{E}}^{*}. \tag{18}$$

3.2.4 Electromagnetic Waves in Matter

In a homogenous, linear dielectric with dielectric constant ε, Maxwell's equations are written as:

$$\begin{aligned} &\text{(i) } \vec{\nabla} \cdot \vec{D} = 0 \quad \text{(iii) } \vec{\nabla} \times \vec{E} = -\frac{\partial \vec{B}}{\partial t} \\ &\text{(ii) } \vec{\nabla} \cdot \vec{B} = 0 \quad \text{(iv) } \vec{\nabla} \times \vec{H} = \frac{\partial \vec{D}}{\partial t} \end{aligned} \tag{19}$$

where $\vec{D} = \varepsilon \vec{E}$ and $\vec{H} = \frac{1}{\mu}\vec{B}$. An electromagnetic wave propagates through a linear homogeneous medium with a speed of:

$$v = \frac{1}{\sqrt{\varepsilon\mu}} = \frac{c}{n} \tag{20}$$

where *n*, the index of refraction of the material, is defined as:

$$n \equiv \sqrt{\frac{\varepsilon\mu}{\varepsilon_0 \mu_0}}. \tag{21}$$

For most materials, $\mu \approx \mu_0$ so:

$$n \cong \sqrt{\frac{\varepsilon}{\varepsilon_0}}. \tag{22}$$

3.2.5 Reflection and Transmission of Electromagnetic Waves

When a wave passes from one transparent medium into another (e.g. air to water) part of the wave is reflected while part of it is refracted into the second medium. The reflection and transmission of these waves depend on the electrodynamic boundary conditions deduced form Maxwell's equations:

$$\begin{aligned} &\text{(i)}\ \varepsilon_1 E_1^{\perp} = \varepsilon_2 E_2^{\perp} \qquad &&\text{(iii)}\ \vec{E}_1^{\parallel} = \vec{E}_2^{\parallel} \\ &\text{(ii)}\ B_1^{\perp} = B_2^{\perp} \qquad &&\text{(iv)}\ \frac{1}{\mu_1}\vec{B}_1^{\parallel} = \frac{1}{\mu_2}\vec{B}_2^{\parallel} \end{aligned} \tag{23}$$

These equations relate the electric and magnetic fields immediately on one side (medium 1) of the interface to that on immediately on the other side (medium 2) of the interface.

Suppose a monochromatic plane wave is incident at an oblique angle at the interface between two linear media (Figure 3).

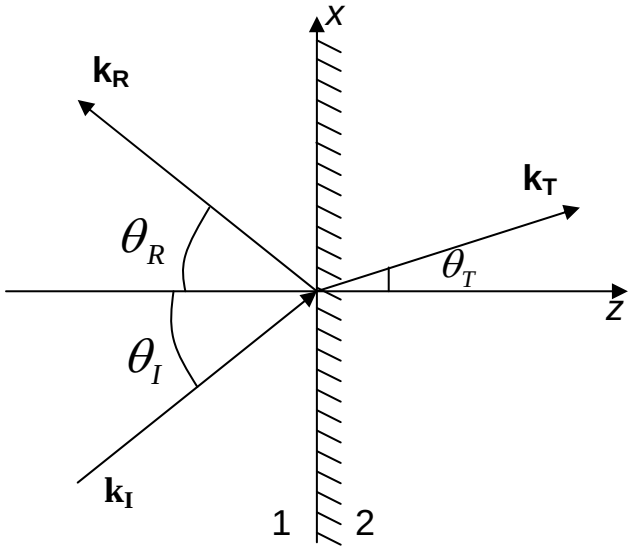

Figure 3: Schematic of electromagnetic wave traveling in medium 1 and incident on medium 2 with an angle with respect to the normal of θ_I .

The monochromatic plane wave incident on the interface from the left is:

$$\tilde{\vec{E}}_I(\vec{r},t)=\tilde{\vec{E}}_{0I}e^{i(\vec{k}_I\cdot\vec{r}-\omega t)} \qquad \tilde{\vec{B}}_I(\vec{r},t)=\frac{1}{v_1}\left(\hat{k}_I\times\tilde{\vec{E}}_I\right). \tag{24}$$

The incident wave results in a reflected wave:

$$\tilde{\vec{E}}_R(\vec{r},t)=\tilde{\vec{E}}_{0R}e^{i(\vec{k}_R\cdot\vec{r}-\omega t)} \qquad \tilde{\vec{B}}_R(\vec{r},t)=\frac{1}{v_1}\left(\hat{k}_R\times\tilde{\vec{E}}_R\right) \tag{25}$$

and a transmitted wave:

$$\tilde{\vec{E}}_T(\vec{r},t)=\tilde{\vec{E}}_{0T}e^{i(\vec{k}_T\cdot\vec{r}-\omega t)} \qquad \tilde{\vec{B}}_T(\vec{r},t)=\frac{1}{v_2}\left(\hat{k}_T\times\tilde{\vec{E}}_T\right). \tag{26}$$

Since all three waves have the same frequency, the wave numbers can be related by:

$$k_Iv_1=k_Rv_1=k_Tv_2=\omega\Rightarrow k_I=k_R=\frac{v_2}{v_1}k_T=\frac{n_1}{n_2}k_T \tag{27}$$

From the boundary conditions (23), the total fields in medium (1), $\tilde{\vec{E}}_I+\tilde{\vec{E}}_R$ and $\tilde{\vec{B}}_I+\tilde{\vec{B}}_R$, must be equal to the fields in medium (2): $\tilde{\vec{E}}_T,\tilde{\vec{B}}_T$. Equations 24-26 all share the same functional form. This implies, at the interface (z = 0), an equation with the generic structure:

$$(\ )e^{i(\vec{k}_I\cdot\vec{r}-\omega t)}+(\ )e^{i(\vec{k}_R\cdot\vec{r}-\omega t)}=(\ )e^{i(\vec{k}_T\cdot\vec{r}-\omega t)}. \tag{28}$$

The parentheses will be filled in a moment. Notice that all the spatial and temporal dependence are in the exponents. These exponential factors must be equal because the boundary conditions hold at all points on the plane for all times. *If not, then a slight change in for example the x direction would destroy the inequality*. Naturally, the time factors are already equal. Thus, for the spatial terms:

$$\vec{k}_I\cdot\vec{r}=\vec{k}_R\cdot\vec{r}=\vec{k}_T\cdot\vec{r}\ ,\ \text{when z = 0} \tag{29}$$

$$\Rightarrow x(k_I)_x+y(k_I)_y=x(k_R)_x+y(k_R)_y=x(k_T)_x+y(k_T)_y$$

which can only hold if the components are separately equal, for example if y = 0, then:

$$\left(k_I\right)_x = \left(k_R\right)_x = \left(k_T\right)_x \tag{30}$$

Since we can orient our axes so that $\mathbf{k_I}$ is in the xz plane we can conclude that the incident, reflected, and transmitted wave vectors form a plane. Furthermore, from Figure 3, equation (30) implies that:

$$k_I \sin\theta_I = k_R \sin\theta_R = k_T \sin\theta_T \tag{31}$$

where θ_I, θ_R, and θ_T are the angles of incidence, reflection, and refraction respectively. From equation (27), we see that the angle of incidence is equal to the angle of reflection, which is the law of reflection. For the angle of refraction we see that:

$$\frac{\sin\theta_T}{\sin\theta_I} = \frac{n_1}{n_2}. \tag{32}$$

This is known as Snell's law. Since the exponential factors in equation (28) are equal they cancel. Thus the boundary conditions, equation (23), become:

$$\begin{aligned}
&\text{(i)}\ \varepsilon_1\left(\tilde{\vec{E}}_{0I} + \tilde{\vec{E}}_{0R}\right)_z = \varepsilon_2\left(\tilde{\vec{E}}_{0T}\right)_z \\
&\text{(ii)}\left(\tilde{\vec{B}}_{0I} + \tilde{\vec{B}}_{0R}\right)_z = \left(\tilde{\vec{B}}_{0T}\right)_z \\
&\text{(iii)}\left(\tilde{\vec{E}}_{0I} + \tilde{\vec{E}}_{0R}\right)_{x,y} = \left(\tilde{\vec{E}}_{0T}\right)_{x,y} \\
&\text{(iv)}\frac{1}{\mu_1}\left(\tilde{\vec{B}}_{0I} + \tilde{\vec{B}}_{0R}\right)_{x,y} = \frac{1}{\mu_2}\left(\tilde{\vec{B}}_{0T}\right)_{x,y}.
\end{aligned} \tag{33}$$

The polarization of the incident electric field can either be parallel or perpendicular to the plane of incidence (the xz plane in Figure 4). Parallel polarization is labeled as *p-polarized* (from the German word parallel), while perpendicular polarization is labeled *s-polarized* (from the German word senkrecht meaning perpendicular). We

will only focus on p-polarized light for the rest of this section because the laser in our experimental setup is p-polarized.

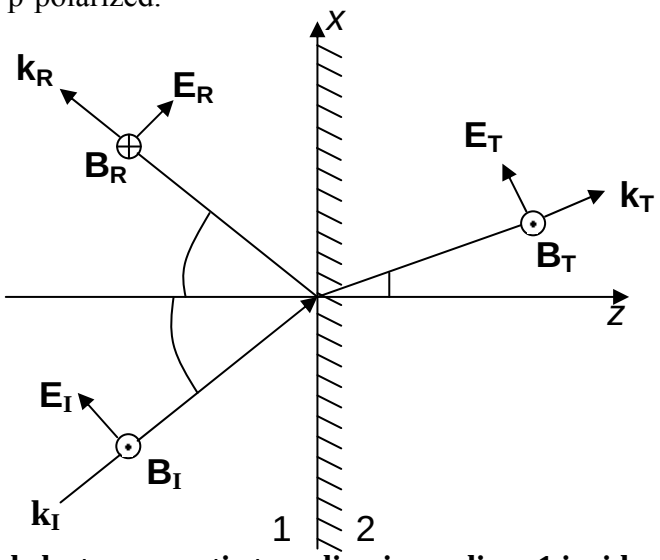

Figure 4: P-polarized electromagnetic traveling in medium 1 incident on medium 2.

For p-polarized light, the boundary conditions (equations 33i, iii, and iv can be written as:

$$\varepsilon_1\left(-\tilde{E}_{0I}\sin\theta_I+\tilde{E}_{0R}\sin\theta_R\right)=\varepsilon_2\left(-\tilde{\tilde{E}}_{0T}\sin\theta_T\right), \tag{34}$$

$$\tilde{E}_{0I}\cos\theta_I+\tilde{E}_{0R}\cos\theta_R=\tilde{E}_{0T}\cos\theta_T, \tag{35}$$

$$\frac{1}{\mu_1 v_1}\left(\tilde{E}_{0I}-\tilde{E}_{0R}\right)=\frac{1}{\mu_2 v_2}\tilde{E}_{0T}. \tag{36}$$

From Snell's law and the law of reflection, equations 34 and 36 reduce to:

$$\tilde{E}_{0I}-\tilde{E}_{0R}=\beta\tilde{E}_{0T} \tag{37}$$

where

$$\beta=\frac{\mu_1 v_1}{\mu_2 v_2}=\frac{\mu_1 n_2}{\mu_2 n_1}\cong\frac{n_2}{n_1} \tag{38}$$

which is a reasonable assumption for most cases (Griffiths 391). Equation 35 says:

$$\widetilde{E}_{0I} + \widetilde{E}_{0R} = \alpha \widetilde{E}_{0T} \tag{39}$$

Where

$$\alpha = \frac{\cos\theta_T}{\cos\theta_I}. \tag{40}$$

Solving equations (37) and (39) for the reflected and transmitted amplitudes, we obtain Fresnel equations for p-polarized light:

$$\widetilde{E}_{0R} = \left(\frac{\alpha - \beta}{\alpha + \beta}\right)\widetilde{E}_{0I} \qquad \widetilde{E}_{0T} = \left(\frac{2}{\alpha + \beta}\right)\widetilde{E}_{0I}. \tag{41}$$

3.3 Total Internal Reflection

Mathematically, it is simplest to discuss total internal reflection (TIR) using plane waves and we will see that plane waves are a good approximation for weakly focused light. From Snell's law (equation 32), when light passes from an optically dense medium into a less dense medium ($n_1 > n_2$) the propagation vector $\mathbf{k_T}$ bends away from the normal (the z-direction in Figure 4). When the angle of incidence reaches a certain critical value, the refracted ray lies along the boundary, having an angle of refraction of 90^o. This angle of incidence is known as the critical angle since it is the largest angle of incidence for which refraction can still occur. Therefore, total internal reflection occurs, when $n_1 > n_2$, for incidence angles θ (measured from the normal to the interface) greater than the *critical angle* θ_c (from Snell's law):

$$n_1 \sin\theta_c = n_2 \sin 90$$

$$\Rightarrow \theta_c \equiv \sin^{-1}\left(n_2/n_1\right) \tag{42}$$

The ratio of the refractive indices (n_2/n_1) must be less than one for TIR to occur. When the incidence angle is less than the critical angle, normal reflection and refraction as

governed by Snell's law, occur. At the critical angle, the angle of refraction of the refracted wave: $\theta_T = 90°$; and thus the transmitted wave grazes the interface. When $\theta_I > \theta_C$, there is no refracted ray and the entire electromagnetic wave is reflected. However, the electric field and magnetic field are not zero in medium 2. As we will see, some of the incident light energy penetrates through the interface and propagates parallel to the surface in the plane of incidence. This part of the wave is known as the evanescent wave, which is quickly attenuated and on average does not transport any energy into medium 2.

3.3.1 Evanescent Field (Transmitted Electric Field)

To describe the evanescent wave mathematically, we see from equation 27 that

$$k_T = \frac{\omega}{v_T} = \frac{\omega n_2}{c}. \tag{43}$$

From Figure 4, it is evident that:

$$\vec{k}_T = k_T\left(\sin\theta_T \hat{x} + \cos\theta_T \hat{z}\right) \tag{44}$$

However, when $\theta_I > \theta_C$:

$$\sin\theta_T = \frac{n_1}{n_2}\sin\theta_I > 1. \tag{45}$$

This implies that the cosine term is imaginary:

$$\cos\theta_T = \sqrt{1-\sin^2\theta_T} = i\sqrt{\sin^2\theta_T - 1}. \tag{46}$$

This indicates that θ_T cannot be interpreted as an angle any more. Many of the interesting properties associated with the evanescent wave are a result of the cosine term in the wave vector being imaginary and we will show that the transmitted electric field is attenuated in the z-direction.

Starting with the general form of the transmitted electric field (equation 26) we solve for the argument in the exponent (using the coordinate axes of Figure 4):

$$\begin{aligned}\vec{k}_T \cdot \vec{r} &= k_T\left(\sin\theta_T \hat{x} + \cos\theta_T \hat{z}\right)\cdot\left(x\hat{x} + z\hat{z}\right)\\ &= k_T\left(\sin\theta_T x + \cos\theta_T z\right)\\ &= \frac{\omega n_2}{c}\left(\frac{n_1}{n_2}\sin\theta_I x + i\left[\sin\theta_T{}^2 - 1\right]^{1/2} z\right)\end{aligned}$$

$$\begin{aligned}&\Rightarrow \vec{k}_T \cdot \vec{r} = \frac{\omega n_1}{c}\sin\theta_I x + i\frac{\omega}{c}\left[\left(n_1\sin\theta_I\right)^2 - n_2^2\right]^{1/2} z\\ &\Rightarrow \vec{k}_T \cdot \vec{r} = k_E x + i\kappa z\end{aligned} \tag{47}$$

where:

$$\begin{aligned}k_E &\equiv \frac{\omega n_1}{c}\sin\theta_I\\ \kappa &\equiv \frac{\omega}{c}\sqrt{\left(n_1\sin\theta_I\right)^2 - n_2^2}\end{aligned}. \tag{48}$$

Thus the transmitted electric field can be written as:

$$\tilde{\vec{E}}_T\left(\vec{r},t\right) = \tilde{\vec{E}}_{0T} e^{i\left(\vec{k}_T\cdot\vec{r}-\omega t\right)} = \tilde{\vec{E}}_{0T} e^{-\kappa z} e^{i\left(k_E x-\omega t\right)}. \tag{49}$$

It is evident that the transmitted wave is propagating in the x-direction and attenuated in the z direction. It can be shown that, when there are no absorbing molecules present in medium 2 to absorb the evanescent field energy, that the reflection coefficient for a TIR light beam is 1 and the transmission coefficient is zero. Using equation 41 we can determine the reflection coefficient. Since α (equation 40) is a function of $\cos\theta_T$, it is imaginary since $\cos\theta_T$ is imaginary (equation 46). Thus we can represent α as *ia* where *a* is a real number and *i* is the imaginary constant and rewrite equation 41 as:

$$E_{0R} e^{i\delta_R} = \left(\frac{ia-\beta}{ia+\beta}\right) E_{0I} e^{i\delta_I} = \tilde{h}\tilde{E}_{0I}. \tag{50}$$

Now the reflection coefficient, R, is given by:

$$R \equiv \frac{I_R}{I_I} = \left(\frac{E_{0R}}{E_{0I}} \right)^2 = \left(\frac{hE_{0I}}{E_{0I}} \right)^2 = h^2 = 1 \tag{51}$$

since:

$$h = \left| \tilde{h} \right| = \frac{\sqrt{\beta^2 + a^2}}{\sqrt{\beta^2 + a^2}} = 1. \tag{52}$$

Similarly we can determine the transmitted evanescent field for p-polarized incident light using equation 41:

$$\tilde{E}_{0T} = \left(\frac{2}{ia + \beta} \right) \tilde{E}_{0I} = \tilde{g} \tilde{E}_{0I}. \tag{53}$$

By combining equations (40) and (46), and incorporating Snell's law we find this expression for *a*:

$$a = \frac{\sqrt{\sin^2 \theta_T - 1}}{\cos \theta_I} = \frac{\sqrt{\dfrac{\sin^2 \theta_I}{\beta^2} - 1}}{\cos \theta_I}. \tag{54}$$

We can now separate $\tilde{g}$ into its real and imaginary parts, $\tilde{g} \equiv g e^{i\delta_p}$, where:

$$g = \frac{2}{\left[a + \beta^2 \right]^{1/2}} \text{ and } \delta_p = \tan^{-1} \left(-\frac{a}{\beta} \right). \tag{55}$$

Also, from Figure 4 we see that:

$$\begin{aligned} \tilde{\vec{E}}_{0T} &= \tilde{E}_{0T} \left(\cos \theta_T \hat{x} - \sin \theta_T \hat{z} \right) \\ &= \tilde{E}_{0T} \left(\frac{1}{\beta} \sqrt{\sin^2 \theta_I - \beta^2} - \frac{1}{\beta} \sin \theta_I \hat{z} \right). \end{aligned} \tag{56}$$

Now, we can solve for the transmitted electric field (equation 49) as a function of the incident angle, θ_I by combining equations (53), (54), (55), and (56) and by assuming incident intensities are normalized to unity (i.e. $\widetilde{E}_{0I} = 1$):

$$\vec{\widetilde{E}}_T = \frac{2}{\left[a^2 + \beta^2\right]^{1/2}} e^{i\delta_p} \left(\cos\theta_T \hat{x} - \sin\theta_T \hat{z}\right) e^{-\kappa z}$$

$$\vec{\widetilde{E}}_T = \frac{2\cos\theta_I}{\left[\sin^2\theta_I - \beta^2 + \beta^4 \cos^2\theta_I\right]^{1/2}} e^{i\delta_p} e^{-\kappa z} \left(i\sqrt{\sin^2\theta_I - \beta^2}\,\hat{x} - \sin\theta_I \hat{z}\right). \qquad (57)$$

Note that the evanescent field vector remains in the plane of incidence (xz plane), but it contains a nonzero longitudinal component (x-direction). The longitudinal component induces the p-polarized light electric field vector to "cartwheel" along the interface and produce elliptical polarization of the evanescent field in the plane of propagation (see Figure 5). When the incident angle is reduced from the supercritical ($\theta_I > \theta_C$) range to below the critical angle, the longitudinal component disappears. The nonzero longitudinal component distinguishes the evanescent field from freely propagating subcritical ($\theta_I < \theta_C$) refracted light, which has no longitudinal component. The evanescent field is a mixture of transverse (z direction) and longitudinal components.

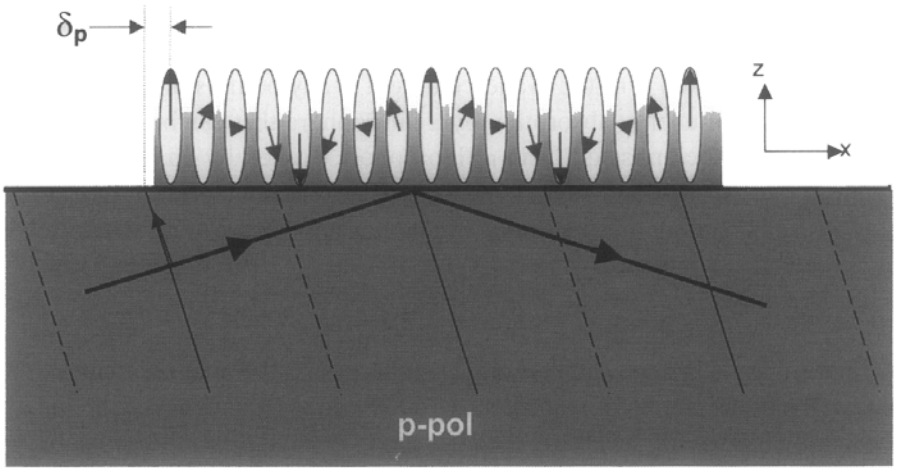

Figure 5: Schematic drawing of the evanescent polarization resulting from p-polarized incident light. The incident light wavefronts determine the spacing of the wavefronts in the evanescent field. The p-polarized evanescent field is elliptically polarized in the x-z plane as shown (mostly polarized in the z-direction with a weaker x-component). Axelrod 2003.

3.3.2 Transmitted Intensity

From the transmitted electric field we can now calculate the transmitted intensity, *I*, as defined by equation (18):

$$\tilde{\vec{E}}_T \cdot \tilde{\vec{E}}^* = \frac{4\cos^2\theta_I}{\left[\sin^2\theta_I - \beta^2 + \beta^4\cos^2\theta_I\right]} e^{i\delta_p} e^{-i\delta_p} e^{-2\kappa z}\left[\left(i\sqrt{\sin\theta_I - \beta^2}\right)\left(-i\sqrt{\sin^2\theta_I - \beta^2}\right) + \sin^2\theta_I\right]$$

$$\Rightarrow I(z) = I(0)e^{-2\kappa z} \tag{58}$$

where:

$$I(0) = \frac{\left(4\cos^2\theta_I\right)\left(2\sin^2\theta_I - \beta^2\right)}{\left[\sin^2\theta_I - \beta^2 + \beta^4\cos^2\theta_I\right]}. \tag{59}$$

Notice that the transmitted intensity is in the form of an exponential decay with perpendicular distance z from the interface. From this it is evident that 1/2κ is characteristic of a penetration depth. Except for the limit as θ approaches the critical angle (where 1/2κ goes to infinity), the penetration depth is of the order of the wavelength of the incident light or smaller. More specifically:

$$\frac{1}{2\kappa} = \frac{\lambda}{4\pi n_1}\left[\sin^2\theta_I - \beta^2\right]^{-1/2} = d \qquad (60)$$

where d is the penetration depth, and λ is the wavelength of the incident electromagnetic wave. We can see that *d* it is independent of the polarization of the incident light and decreases with increasing θ.

The p evanescent intensity *I(0)* is plotted versus the incident angle, θ_I in Figure 6 for transmitted light in the lower refractive index when passed through an interface composed of glass ($n_1 = 1.52$) and water or an aqueous buffer solution ($n_2 = 1.33$). Intensity, plotted on the ordinate, is expressed as the ratio of evanescent intensity at the interface to the incident intensity. As you can see, the evanescent intensity approaches zero as the incident angle goes to 90^o. Conversely, for supercritical angles within 10^o of the critical angle, it is interesting to note that the evanescent intensity exhibits a range between one and five times that of the plane wavefront incident intensity. The plots can be continuously extended to the subcritical angle range, where the intensity is that of the freely propagating refracted light in medium 1. From Figure 6, it appears that the intensity of the refracted light (when $\theta_I < \theta_C$) is greater than the intensity of the incident light. This is because the intensity in Figure 6 refers to EE^* alone and not the actual energy flux of the light, which would involve a product with the refractive index of the medium in which the light propagates.

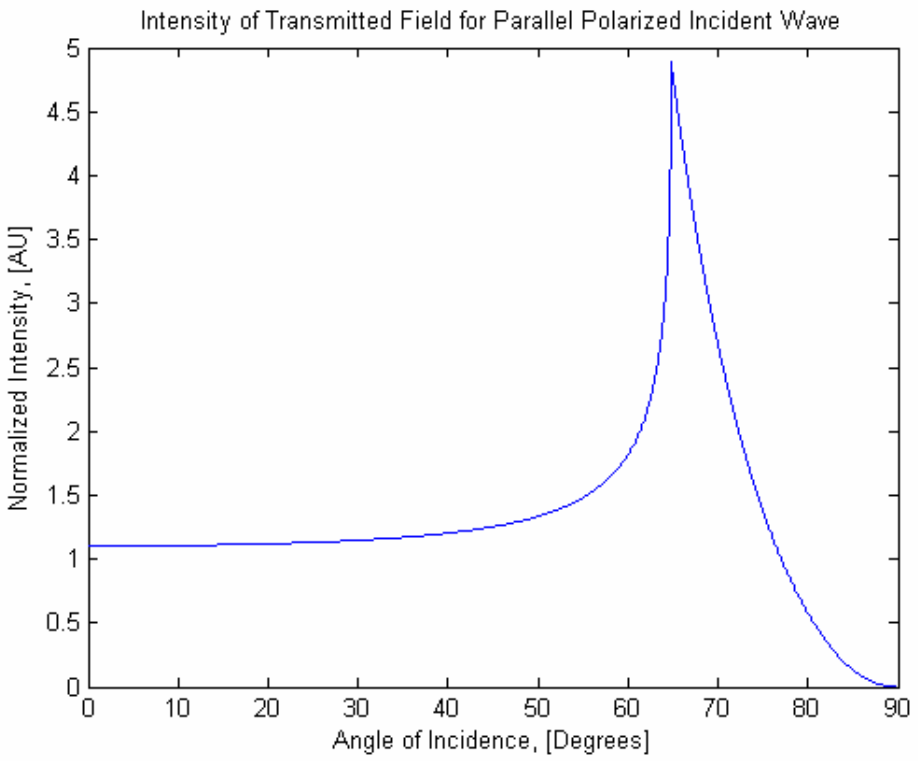

Figure 6: Intensity (EE^*) versus incidence angle. This graph was made with the same experimental parameters in our setup (see Appendix III for MATLAB Code).

3.4 Finite Width Beams

The discussion thus far has been limited to plane waves. In reality, the incident is not a plane wave but rather a finite-width incident beam. For finite-width incident beams, the incidence angle dependence of the phase factor δ_p gives rise to a measurable longitudinal shift of the beam, known as the Goos-Hanchen shift. This shift ranges from a fraction of a wavelength at $\theta = 90°$ to infinite at $\theta = \theta_c$, which corresponds to the refracted beam skimming along the interface. A finite incidence beam can be expresses as a weighted integral over infinite plane waves approaching at a range of incidence angles; each plane wave at each angle gives rise to its own exponentially decaying evanescent field of infinite lateral extent. The x-y intensity profile of the evanescent field for the finite beam can then be calculated by the weighted integral of these plane-wave-

generated evanescent fields over the range of incident plane-wave angles. For a totally internally reflected Gaussian laser beam focused with a typically narrow angle of convergence, the evanescent illumination is approximately an elliptical Gaussian profile, and the polarization and penetration depth are approximately equal to those of a single infinite plane wave (Burghardt & Thompson 1984).

4 Methods

4.1 Experimental Setup

To maximize the signal to noise ratio in our spectra, we designed a prism-based total internal reflection fluorescence (TIRF) microscope which will serve as a platform for Raman scattering experiments from supported bilayers. In our setup, a prism (glass) (obtained from Casix) is placed on top of the sample chamber which is on top of an inverted microscope. A laser beam is incident on the prism with an angle of incidence greater than the critical angle such that the incident beam will be reflected entirely. With total internal reflection, there is an evanescent wave which propagates along the interface and extends into the sample with a penetration depth of about 100nm. It is this evanescent wave that excites the molecules in our sample.

The use of a high-aperture objective (greater than N.A. 1.4), without a prism, can also be used to simultaneously direct illumination to the interface and capture secondary fluorescence emission produced by the sample. However, we chose to use a prism-based setup because the amount of scattered light from the excitation path entering the objective is significantly minimized, especially when compared with objective based TIR.

A tunable Ar^+ laser (set at 488 nm) (Melles Griot 43 series ion laser) is used to excite TIR fluorescence in our sample. A periscope, consisting of a pair of mirrors, is used to raise the Ar^+ beam to ~22cm above the optical table (see Figure 8). A lens (LMR2 Thor Labs) (f = 20 cm) is then used to focus the laser beam onto the sample, which is placed on the stage of a Nikon inverted microscope (TE-2000U). A 60X water-immersion objective (Nikon, NA 1.00) with a working distance of 2.00 mm is used to for imaging the scattered light from the sample onto the entrance slit of an Acton SP2300-I

imaging spectrograph with an EEV chip (1340 x 100 pixels). It is necessary to use an objective with a relatively large working distance because we need to be able to focus on the top of the sample chamber, where TIR is occurring. A Roper Scientific Spec 10 CCD camera is used to record the fluorescence spectra, of our sample. A Ti:Sapphire (Spectra Physics Model 3900s), pumped by a frequency doubled Nd:VO_4 laser (Spectra Physics Millenia Xs) is co-aligned with the Ar^+ laser (Figure 7). The Ti:Sapphire beam is used to excite Raman scattering from our sample. With an intensity of about 1.15 watts the Ti-Sapphire laser is an order of magnitude more intense than the Ar^+ laser and thus can obtain higher signal to noise ratios. Furthermore, the use of near infrared excitation (the Ti-Sapphire laser is tuned to 750 nm) minimizes the amount of fluorescence noise from impurities in the buffer (discussed later).

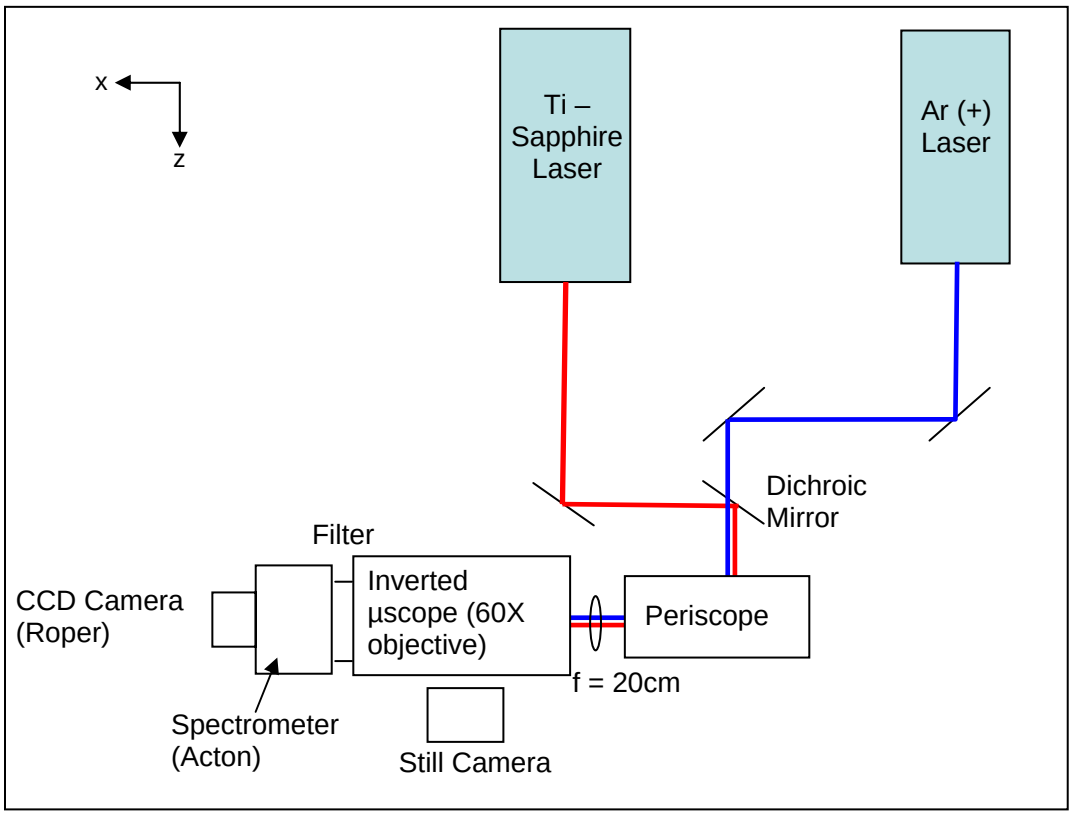

Figure 7: Basic Setup Block Diagram.

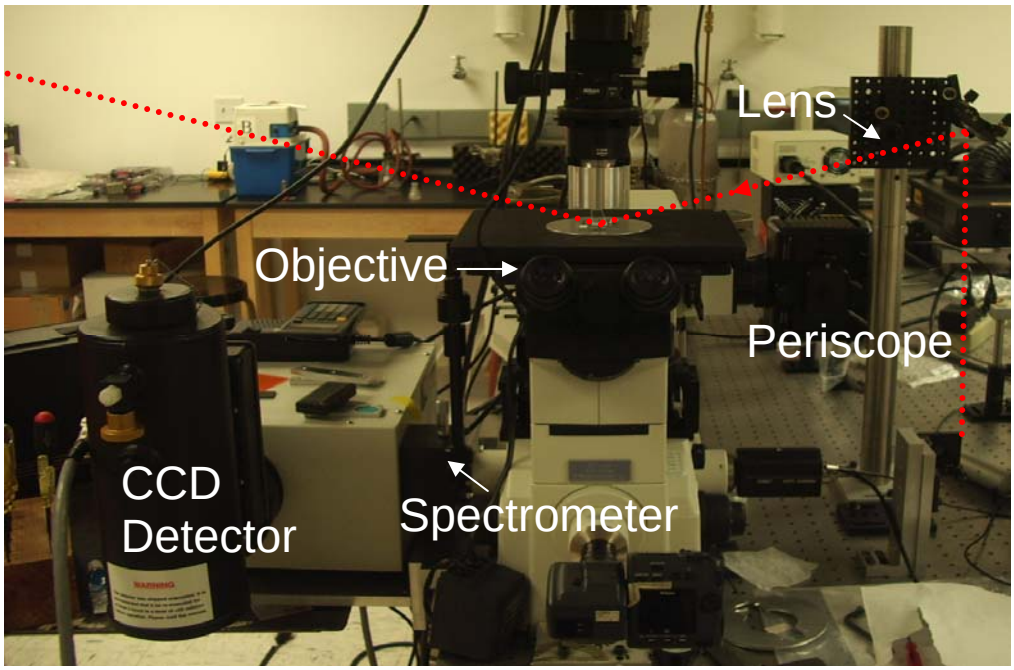

Figure 8: Experimental apparatus (·····) represents path of laser beam

As Figure 8 depicts, the laser beam is brought off the optical table and focused onto the sample by a pair of mirrors. The top mirror allows us to adjust the position where the laser beam is focused on the sample. The scattered light is collected through the objective and a long pass filter with 99% transmission. The filter (HQ 760 LP, Chroma) is used to filter out incident laser light that is scattered into the objective.

4.2 Sample Preparation

Of the different types of lipid bilayer systems, we chose to use solid supported lipid bilayers as our system. Phospholipid bilayers supported by solid substrates are more robust and stable than other methods for forming bilayers (e.g. black lipid membranes) (Castellana & Cremer 2006). More importantly, our total internal reflection excitation setup has been designed to analyze supported bilayers. In solid supported systems membrane fluidity is maintained by a 10-20 Å layer of trapped water between the

substrate and the bilayer (Tamm & McConnell 1985). A schematic diagram of a supported bilayer is shown in Figure 9.

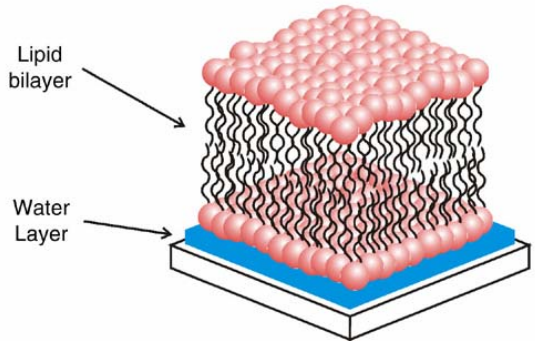

Figure 9: Schematic diagram of a solid supported phospholipid bilayer. The bilayer is separated form the substrate by a 10-20 Å thick layer of water. (Castellana & Cremer 2006)

Traditionally supported bilayers have been made using the Langmuir-Blodgett technique. However, because of our lack of access to a Langmuir-Blodgett trough, we used the much easier vesicle fusion technique. The adsorption and fusion of unilaminar vesicles on quartz (Frey & Tamm 1992) is one of the easiest and most versatile means for forming solid supported phospholipid bilayers. The physical properties of these supported bilayers are shown to be identical to those created by the Langmuir-Blodgett deposition technique. Furthermore, small unilamellar vesicles (SUVs) are readily made by the use of a small-volume extrusion apparatus, outlined in Macdonald *et. al* 1991.

The model bilayers used for our studies were made with two lipids: 1-Palmitoyl-2-Oleoyl-*sn*-Glycero-3-Phosphocholine (POPC) and 1,2-Dipalmitoyl-*sn*-Glycero-3-Phosphoethanolamine-N-(7-nitro-2-1,3-benzoxadiazol-4-yl) (NBD-DPPE), (Figure 10). Phosphatidylcholines are a major component of cell membranes; therefore POPC is a good representation of lipids in cell membranes. POPC contains a completely saturated fatty acid (palmitic acid) and a fatty acid with one double bond (oleic acid). The

fluorescent dye NBD is covalently attached to the head group of DPPE, which contains two saturated fatty acids, to create NBD-DPPE.

The procedure to prepare the lipid for extrusion was adapted from McDonald et al. and is as follows: 60µL 10mM POPC in chloroform and 10µL 1 mg/mL NBD-DPPE (2 % mole fraction) in chloroform (Avanti Polar Lipids) are dried under nitrogen and kept under vacuum for an hour. The lipid is then hydrated with 700µL of a buffered (pH 7.4) solution containing 10 mM KCl and 20mM HEPES and freeze-thawed 5 times in a liquid nitrogen bath. The multilamellar vesicles were then extruded through two polycarbonate filters (100 nm pore diameter) mounted in the mini extruder (Avestin LiposoFast) fitted with two 1.0 mL syringes. The sample is usually subjected to at least 13 passes through the extruder. An odd number of passages are performed to avoid contamination of the sample by large vesicles which might not have passed through the filter. The vesicles created from this technique are of uniform size and are unilamellar.

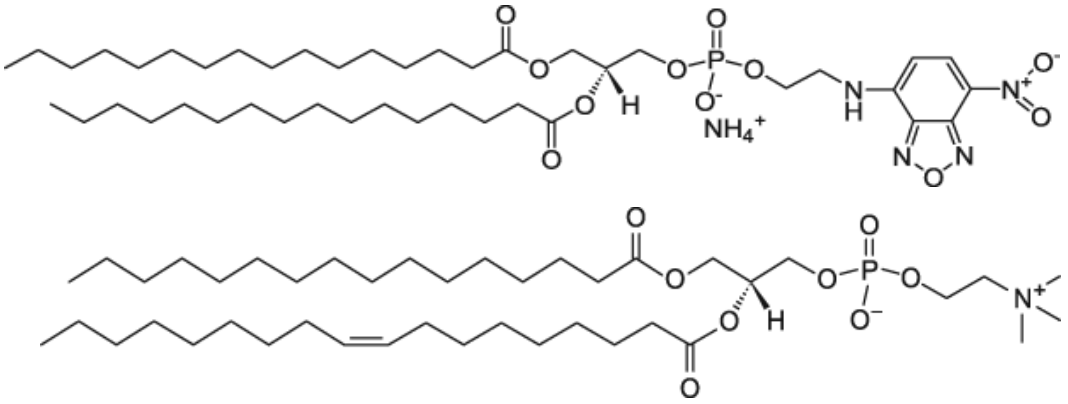

Figure 10: Molecular structures of POPC (bottom) and NBD-DPPE (top). Images obtained from Avanti Polar Lipids website (http://www.avantilipids.com/index.htm, accessed April 2009)

The 0.1 mM suspension of small unilamellar vesicles formed by extrusion is injected into a flow through chamber (see Figure 11) and incubated for 45 minutes to an

hour so that the SUV's spontaneously rupture and fuse to the quartz surface. The chamber is then flushed with 10 mL of water to wash away excess vesicles, leaving a single bilayer on the quartz surface.

The flow through chamber consists of a ~1.5 mm layer thick of liquid sandwiched by a quartz microscope slide (~1 mm thick) and a glass coverslip (~0.15 mm thick) at the bottom (Figure 11). The chamber walls are defined by a hollowed out Teflon spacer that is 1.5 mm thick with access ports for filling and draining fluid via hypodermic needles. An aluminum frame clamps the quartz slide, Teflon spacer, and glass coverslip together to form the sample chamber.

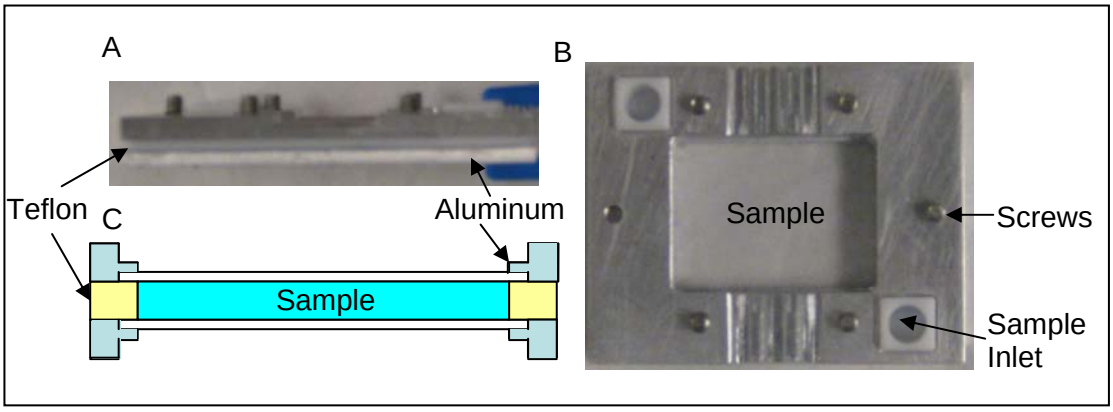

Figure 11: Sample Chamber. (A) Side picture of sample chamber. (B) Top view of sample chamber. (C) Cross-sectional schematic of sample chamber.

Quartz slides were cleaned by immersion in three volumes of 95% H_2SO_4 to one volume of 30% H_2O_2 for 1 h followed by extensive rinsing in water. Cleaned slides were stored in a sheltered beaker of water.

4.3 Prism Design

The prism is designed to ensure that total internal reflection occurs at the sample, i.e. the bilayer-water interface inside of the sample chamber. Several different aspects need to be considered in deciding on the optimal angle for the prism. The angle of the prism is important because it determines the angle of incidence of the laser beam. Normal incidence of the laser beam on the prism greatly simplifies the experimental reproducibility of the setup because it is straightforward to align the beam such that normal incidence is occurring. We decided to use an angle of incidence of 74^{o} in order to optimize the signal to noise ratio from our sample. As the angle of incidence of the TIR excitation beam increases above the critical angle, the intensity of the evanescent field used for TIR excitation decreases (see Figure 6) and thus both the signal and noise decrease. However, as the angle of incidence increases, the noise decreases because the penetration depth of the evanescent wave decreases (equation 60). For example, with a laser wavelength of 750 nm, the penetration depth for incident laser light at an angle of incidence just above the critical angle ($\sim 62^{o}$) would yield a penetration depth of ~330 nm. An incident angle of 74^{o} would yield a penetration depth of ~98 nm. A smaller penetration depth results in less noise because a lipid bilayer is approximately 5 nm thick and the greater percentage the lipid bilayer makes up of the imaging slice the greater the signal to noise ratio. By making the prism at an angle larger than the critical angle we are attempting to maximize the signal to noise ratio in anticipation of the Raman spectra.

4.4 Alignment of the TIR System

1) We glued (Duco Cement) the prism to an aluminum cylinder which fits into the condenser mount of the microscope (see Figure 8). The prism is fixed in the plane of the

sample but has movement in the vertical direction. Note that it is necessary for the prism to lay directly in the optical axis of the microscope objective.

2) It is necessary to have a system of mirrors with adjustable angle mounts (a periscope in our case) fixed to the optical table so that the beam can be directed toward the prism. Furthermore, a mechanism in which it is possible to switch between epifluorescence illumination and total internal reflection is desired. The epifluorescence excitation source and the TIRF laser source should be in comparable wavelength regions so they can excite the same sample. Our microscope is equipped with Mg lamp epifluorescence.

3) For the rough alignment of the incident laser beam, we make sure that the laser beam is approximately incident in the optical axis of the microscope objective.

4) The sample chamber is then placed with the NBD labeled lipid bilayer on the microscope stage. To ensure that the objective is focusing on the right plane of the sample chamber (i.e. the top interface between the quartz coverslip and the sample) we focus using epifluorescence. The emission is filtered through a low pass filter (> 520 nm) to make certain that we are only observing fluorescence. Note that focusing on the right plane of the sample is not trivial. From Figure 12 it is evident that there are at least two possible focal planes: the sample quartz interface and the sample glass interface. However, we found that there are actually three focal planes: two very close each other near the sample glass interface and one at the sample quartz interface (we are not sure why this is).

5) In order to optically couple the prism to the quartz coverslip, some type of index matching fluid is used. We place a small drop of glycerol on the quartz coverslip and carefully translate the prism vertically so it touches and spreads the oil, but does not

squeeze it so tightly that lateral sliding motion is inhibited. Too much oil will bead up around the edges of the prism and interfere with the excitation path.

6) By eye we adjust the focused laser beam position with the mirrors so that total internal reflection occurs directly in line with the objective's optical axis. This can be seen by the scattering of the fluorescence from the sample.

7) The placing of the prism on the sample might have moved the sample enough to slightly alter the focal plane. Re-focusing using epifluorescence is usually done at this step to make sure that the objective is focusing on the right plane.

8) The TIR region should now be positioned relatively close to the field of view of the microscope such that only minor adjustments are needed to observe the TIR region. It is necessary that the field of view of the microscope objective is overlapping with the TIR region. When they overlap, you can observe the scattering of the incident laser beam off the imperfections (i.e. scratches) of the quartz microscope slide. Furthermore if TIRF is occurring, the TIR region will appear as a colored (depending on dye used) ellipse or streak with a region of discrete tiny bright dots. It is clearly evident when you are observing a TIR region through the microscope because slight alterations of the position of the incident layer will cause the TIR region to disappear.

4.5 Observing TIRF: Angle of Incidence Corrections

In the theory section of this report, two media TIR was only considered. In actuality our interface is not simply between two media, but rather a three layer system as indicated in Figure 12. In order for the prism to be optically coupled to the sample chamber we inserted a thin layer of glycerol (n = 1.47). Index matching fluid is

necessary because unevenness in the prism/quartz surface would lead to air gaps, which would distort the beam before it reaches the sample interface. Axelrod stated that since the intermediate layer is likely to be very thin (no deeper than several tens of nanometers), precisely which interface supports TIR is not important for qualitative studies. The only question is whether TIR takes place at the n_1-n_2 interface or the n_2-n_3 interface (assuming for now that the quartz coverslip and glass prism have approximately the same index of refraction.

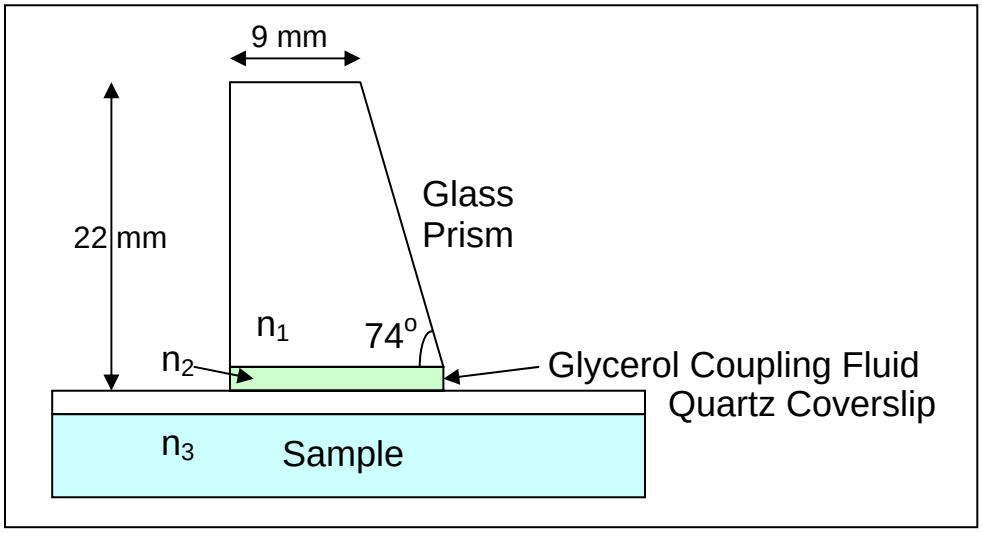

Figure 12: Cross-sectional schematic of the different layers of our system. Figure not drawn to scale.

However, we believe that the intermediate glycerol layer in our system is important in observing TIR. An angle of incidence of 74° is very close to the critical angle (75°) for the prism-glycerol interface. We believe TIR at this interface was the reason we were not able to observe TIR at an incident angle of 74°. When we decreased the angle of incidence below the critical angle of the prism-glycerol interface we were able to observe TIR which suggests our beliefs to be correct. The optimal angle of incidence we settled at was approximately 68° (Figure 13).

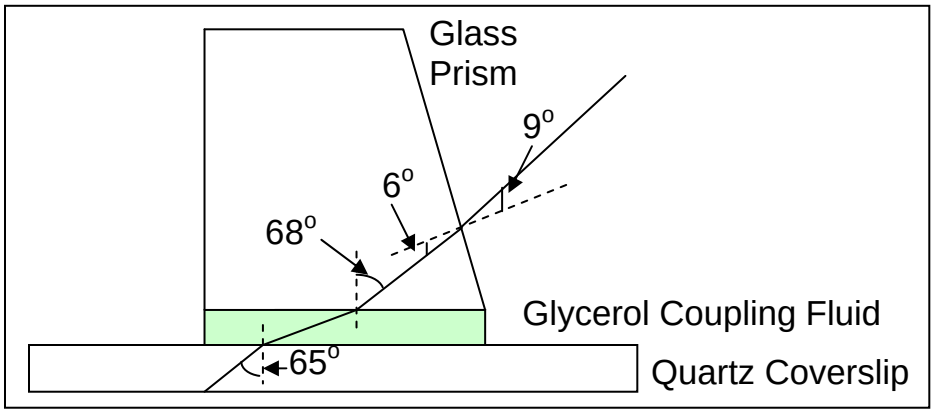

Figure 13: Schematic of the important reflections and refractions of prism system when the incident laser beam is adjusted such that there will be an incidence angle of 68° at the prism-glycerol interface. Figure not drawn to scale.

4.6 Collecting Spectra

The fluorescently labeled lipid bilayer collected by the 60x water-immersion objective is imaged onto the entrance slit of a spectrograph (Acton SP-2300) opened to 50 μm. A high pass filter (HQ 520 LB, Chroma Tech) is inserted into the beam path to reduce the amount of inelastically scattered light from the Ar^+ laser. The spectra are recorded by a liquid Nitrogen-cooled CCD camera (Roger Scientific Spec10).

The spectrograph was initially calibrated with a Neon arc lamp. Winspec 32, supplied by Roper Scientific, is used to control the integration time, the angle of gratings in the spectrograph, and the temperature of the CCD camera. The data was collected using a 600 groves/mm CCD grating.

4.7 Qualitative Fluorescence Recovery after Photobleaching

Fluorescence recovery after photobleaching (FRAP) is a widely used optical technique that assess the two dimensional fluidity of a lipid bilayer containing fluorescently labeled probes. The property of fluorophores to photobleach, the process in which a fluorophore is photochemically destroyed, is exploited in FRAP to study the

diffusion of molecules. In short, a small region of a bilayer of uniform fluorescence intensity receives high intensity illumination, which causes the photobleaching of this region and the observation of a noticeable dark spot. As Brownian motion proceeds, the still-fluorescing probes will diffuse throughout the sample and replace the non-fluorescent probes in the bleached region. In most applications, the recovery of intensity is quantitatively monitored allowing for the analytical determination of the diffusion constant from fitting the data to the diffusion equation. To do this, the fluorophore must be covalently attached to the molecule of interest (in our case the fluorophore NBD is attached to the DPPE lipid).

However, we only used FRAP to qualitatively assess the fluidity of the lipid bilayers formed. Qualitative FRAP provided us with a fast and easy way of determining whether or not a supported lipid bilayer was formed. The FRAP procedure used is as follows:

1) Formation of POPC supported lipid bilayer with uniformly labeled fluorescent probes (NBD-DPPE).

2) A pinhole in the beam path of the epifluorescence excitation source, which is conjugate to the object plane (i.e. plane in focus), can be adjusted so as to selectively excite a region within the field of view of the plane in focus. Excitation for ~10 seconds is sufficient to photobleach this region. Expanding the pinhole region will allow for the observation of a dark spot the size made from the previous pinhole region.

3) A shutter on the microscope is then closed to block the access of the excitation light to the sample. The shutter is closed for ~ 1 min.

4) The shutter is opened and the photorecovery of the lipid bilayer is assessed via eyes.

5 Results

5.1 TIRF Spectra

When NBD-DPPE lipids are excited with around 460 nm (excitation peak) light, they have a broad, smooth characteristic fluorescence spectrum in the 500-600 nm region. A representative total internal reflection fluorescence (TIRF) spectrum of a planar supported lipid bilayer with POPC and NBD-DPPE excited with an Ar^+ (488 nm) laser is shown in Figure 14. This spectrum shows that the TIRF setup is functional since the spectrum is characteristic of fluorescence from the NBD labeled lipid which contains a fluorescence maximum at 550 nm.

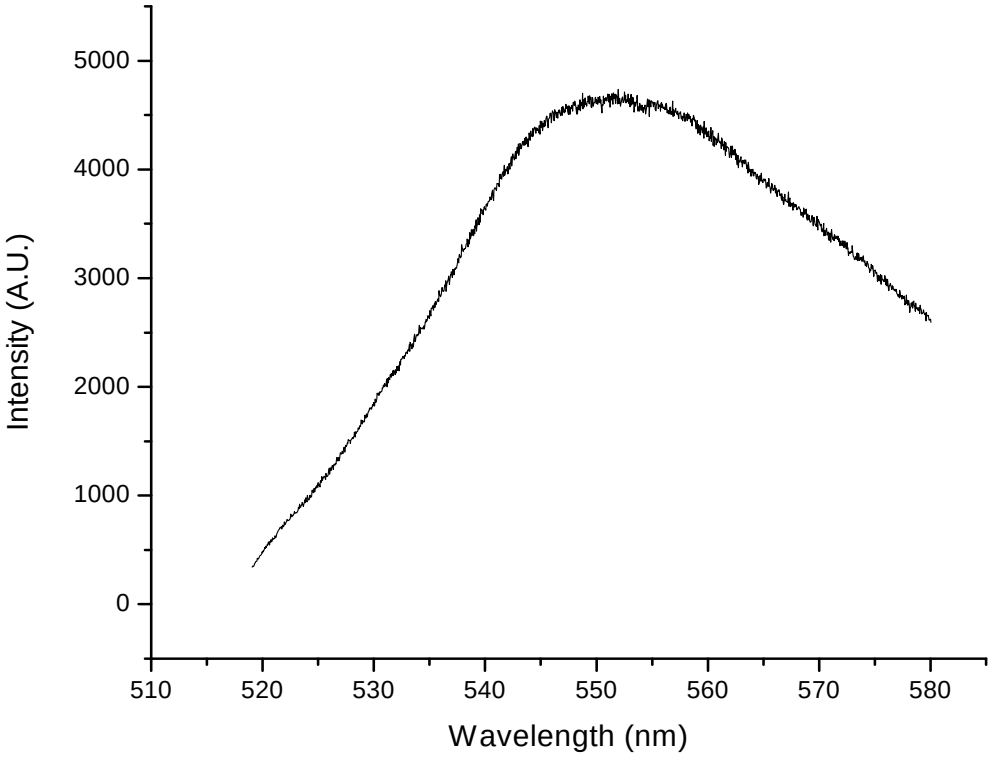

Figure 14: TIRF spectrum of POPC and NBD-DPPE planer lipid bilayer. TIR region is centered directly on the field of view of the objective.

5.2 Images of Supported Bilayer

Using the Basler (A311f) camera attached to the microscope we obtained images of the qualitative fluorescence recovery after photobleaching (FRAP) experiments done to assess the fluidity of the bilayer. Figure 15A is the bilayer before photobleaching and Figure 16B shows a photobleached region of the bilayer. These images indicate that the sample is not just fluorescent molecules in solution because fluorescent molecules in solution would be moving much too rapidly to obtain a clear photobleached image. The presence of photobleaching like that of Figure 16B indicates that there are fluorescent molecules attached to the quartz substrate which is suggestive of a bilayer. The true test of whether or not the sample is indeed a bilayer is that the photobleached region should be able to recover after an amount of time characteristic of diffusion in a typical bilayer. A probe diffusion constant in between 0.5 – 5.0 μm/s are typical values reported for fluid bilayers in previous studies (Lee & Jacobson 1994). About half of the supported lipid bilayer samples we created were able to recover after photobleaching (images not shown).

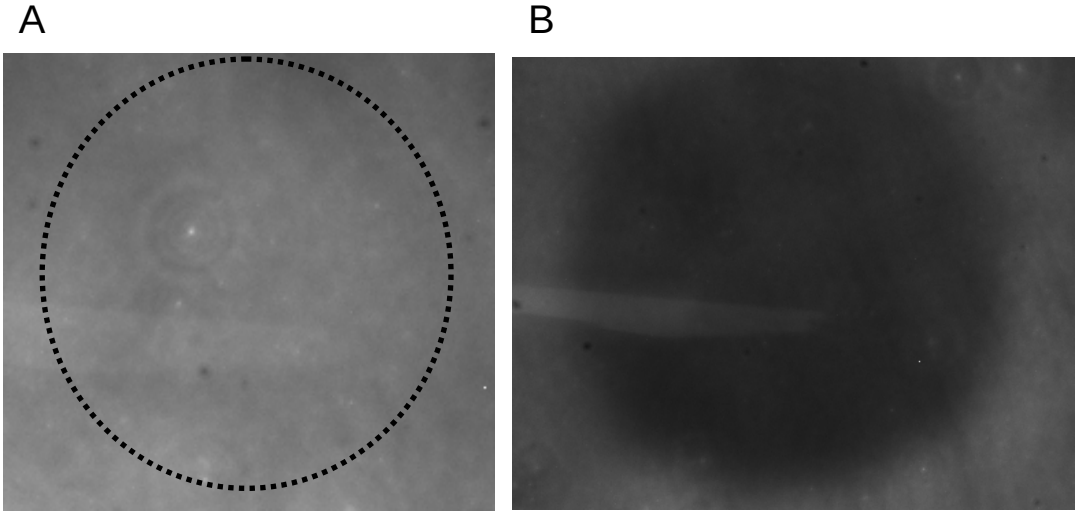

Figure16: Photobleaching of lipid bilayer. (A) Image of bilayer before it has been photobleached. Dashed line indicated region of photobleaching. (B) image of bilayer with a region of photobleaching.

6 Discussion

The successful construction of a TIRF microscope was demonstrated in this study. The signature signs of total internal reflection were observed. In the TIR region the scratches on the quartz coverslip were visible; a fluorescent streak was also visible when the filter is in place; the intensity of the fluorescence and the ability to observe the scratches of the coverslip are very sensitive to the location of the incident beam. Slight alterations in the beam's location will cause the TIR region to disappear.

The Ar^+ laser that was used in this study is suitable for fluorescence studies because it is in the region of excitation for the dye we are using (and also rhodamine) and can thus be used alongside the epifluorescence mercury lamp on the microscope. However, since the maximum power of the Ar^+ laser is only ~100 mW, it is not suitable for Raman imaging experiments. We will therefore use a Ti:Sapphire laser with maximum power of ~1 W, for future TIR Raman studies.

Now that we have a functioning TIR microscope and a suitable method of making and analyzing supported lipid bilayers, the stage is set for future experiments. We will now be able to perform Raman spectral imaging experiments on different lipid bilayer systems. In the future we hope that we will be able to have developed a technique that will allow for the quantitative determination of lipids in an unknown binary system. Eventually this setup could perform the first experiments to quantitatively determine the lipid composition and concentration of lipid domains. Even further down the line this setup could be used to study the distribution of domains in asymmetric lipid bilayers. In short, with the functioning TIR excitation microscope developed in this study, there are a large variety of novel important experiments that can be performed on supported bilayers.

7 Conclusion

We have developed a TIRF microscope that will be the framework for TIR Raman experiments on supported lipid bilayers. TIRF was demonstrated by the observation of enhanced fluorescence intensity of a lipid bilayer with a certain percentage of fluorescently labeled head groups. This setup is the foundation for future experiments that will for once elucidate quantitatively the composition of lipid domains in model membranes.

8 Appendix

8.1 Appendix I**:** Derivation of equations (12) and (13)

Maxwell's equations make up a set of coupled, first-order, partial differential equations for **E** and **B**, which can be decoupled by applying the curl to (iii) and (iv):

$$\vec{\nabla}\times\left(\vec{\nabla}\times\vec{B}\right)=\vec{\nabla}\left(\vec{\nabla}\cdot\vec{E}\right)-\nabla^2\vec{E}=\vec{\nabla}\times\left(-\frac{\partial\vec{B}}{\partial t}\right)=-\frac{\partial}{\partial t}\left(\vec{\nabla}\times\vec{B}\right)=-\mu_0\varepsilon_0\frac{\partial^2\vec{E}}{\partial t^2}$$

$$\vec{\nabla}\times\left(\vec{\nabla}\times\vec{B}\right)=\vec{\nabla}\left(\vec{\nabla}\cdot\vec{B}\right)-\nabla^2\vec{B}=\vec{\nabla}\times\left(\mu_0\varepsilon_0\frac{\partial\vec{E}}{\partial t}\right)=\mu_0\varepsilon_0\frac{\partial}{\partial t}\left(\vec{\nabla}\times\vec{E}\right)=-\mu_0\varepsilon_0\frac{\partial^2\vec{B}}{\partial t^2}$$

Since $\vec{\nabla}\cdot\vec{E}=0$ and $\vec{\nabla}\cdot\vec{B}=0$,

$$\nabla^2\vec{E}=\mu_0\varepsilon_0\frac{\partial^2\vec{E}}{\partial t^2}\qquad\nabla^2\vec{B}=\mu_0\varepsilon_0\frac{\partial^2\vec{B}}{\partial t^2}.$$

This gives us second order separate equations for E and B. These equations satisfy the three-dimensional wave equation:

8.2 Appendix II: Derivation of equation (15):

$$\widetilde{S}\equiv\frac{1}{\mu_0}\left(\widetilde{E}\times\widetilde{B}\right)$$

$$\widetilde{S}=\frac{1}{c\mu_0}\widetilde{E}\times\left(\hat{k}\times\widetilde{B}\right)=\frac{1}{c\mu_0}\left\{\hat{k}\left(\widetilde{E}\cdot\widetilde{E}^*\right)-\widetilde{E}\left(\widetilde{E}\cdot\hat{k}\right)\right\}$$

From vector identities (Griffiths).

But, $\widetilde{E}$ is the same direction as $\hat{n}\Rightarrow\widetilde{E}\cdot\hat{k}=0$ since $\hat{n}\cdot\hat{k}=0$ because the polarization vector is perpendicular to the wave vector for transverse waves. Thus:

$$\widetilde{\vec{S}}=\frac{1}{c\mu_0}\left(\widetilde{\vec{E}}\cdot\widetilde{\vec{E}}^*\right)\hat{k}$$

8.3 Appendix III: Matlab Code for Intensity plot

```
% tot_int_ref_par.m
%
% This routine uses the Fresnel Equations (see page 390 and Problem 9.37
% in the text "Introduction to Electrodynamics", 3rd Edition,
% by David J. Griffiths) to solve for the intensity of the transmitted
% wave, assuming that the incident wave is polarized parallel to the
% plane of incidence.
%
% Note that, for angles of incidence greater than the critical angle
% (see below), the EM waves exhibit the phenomena of total internal
% reflection and an evanescent wave (Griffiths, Problem 9.37).
%
% Kevin Kelley, 11/29/08
%**************************************************************************

% Define values for the physical paramters of the system.
n1 = 1.47;          % Refractive index of media 1
n2 = 1.33;          % Refractive index of media 2
thc = asin(n2/n1);   % Critical angle, [rad]
lambda = 750e-9;     % Wavelength of incident field, [m]

% Calculate and plot the transmitted intensity for angles of incidence less
% than the critical angle.  Note that the intensity is normalized by the
% incident E-field => I = (EoT/EoI)^2 = (2/(alpha+beta))^2 (Griffiths, 9.109)
thI_div = 0.05*(pi/180);                    % Input angles of incidence, divisions, [rad]
thI = [0:thI_div:thc];                      % Input angles of incidence, [rad]
sinthI = sin(thI);                          % Vector of sines of thI
costhI = cos(thI);                          % Vector of cosines of thI
sinthT = (n1/n2)*sinthI;                    % Vector of sines of thT
costhT = sqrt(ones(size(thI))-sinthT.*sinthT); % Vector of cosines of thT
alpha = costhT./costhI;                     % Vector of alpha's (Griffiths, 9.108)
beta = ones(size(thI))*(n2/n1);             % Vector of beta's (Griffiths, 9.106, with mu1 = mu2)
alphapbeta = (alpha+beta);                  % Vector of alpha+beta
EoTnorm = 2*ones(size(thI))./alphapbeta;    % Vector of normalized transmitted field, (EoT/EoI)
(Griffiths 9.109)
I = EoTnorm.*conj(EoTnorm);                 % Vector of normalized intensity, (EoT/EoI)^2 (Kelley
thesis)
figure(1)
plot(thI*(180/pi),I);
axis([0 90 0 5]);
xlabel('Angle of Incidence, [Degrees]'); ylabel('Normalized Intensity, [AU]');
title('Intensity of Transmitted Field for Parallel Polarized Incident Wave')
hold on

% Calculate and plot the transmitted intensity for angles of incidence greater
% than the critical angle, and for various fractions of distance, z, with respect to the
% incident wavelength, lambda.  Note that the intensity is normalized by the
% incident E-field => I = (EoT/EoI)^2 = (2/(alpha+beta))^2 (Griffiths, 9.109)
thI = [thc:thI_div:pi/2];                   % Input angles of incidence, [rad]
sinthI = sin(thI);                          % Vector of sines of thI
costhI = cos(thI);                          % Vector of cosines of thI
sinthT = (n1/n2)*sinthI;                    % Vector of sines of thT
costhT = sqrt(ones(size(thI))-sinthT.*sinthT);          % Vector of cosines of thT
```

```
alpha = costhT./costhI;                          % Vector of alpha's (Griffiths, 9.108)
beta = ones(size(thI))*(n2/n1);                  % Vector of beta's (Griffiths, 9.106, with mu1 =
mu2)
alphapbeta = (alpha+beta);                       % Vector of alpha+beta
kappa = (2*pi*n1/lambda)*sqrt(sinthI.*sinthI-beta.*beta); % Vector of kappa's (Griffiths, 9.202 and
Kelley thesis)
z = [0 0.2 0.4]*lambda;                          % Input depth distances, [m]
for j = 1:length(z),
   EoTnorm = (2*ones(size(thI))./alphapbeta).*exp(-kappa*z(j)); % Vector of normalized
transmitted field, (EoT/EoI) (Griffiths 9.109)
   I = EoTnorm.*conj(EoTnorm);                   % Vector of normalized intensity,
(EoT/EoI)^2 (Kelley thesis)
   plot(thI*(180/pi),I);
end;
grid;
hold off
```

9 Acknowledgements

Thank you Glenn Flohr for all your help with the design and machining of the prism mounts and sample chambers. Thank you David Haley for helping us find anything we needed (vacuum pump and tubes, elevator thingy, and the LN doer).

I would also like to thank the Pomona College Physics department for support and the Chemistry department for various supplies (especially the liquid nitrogen!).

Lastly, I would like to thank Professor Kwok for all his help and guidance in every step of the way.

10 Works Cited

Axelrod, D. (2001). Total internal reflection fluorescence microscopy in cell biology. *Traffic,* 2: 764-774.

Axelrod, D. (2003). Total internal reflection fluorescence microscopy in cell biology. *Biophotonics, Pt B, 361*, 1-33.

Brugger B, Graham C, Leibrecth I, Mombelli E, Jen A, Wieland F, Morris R (2004). The membrane domains occupied by glycosylphosphatidylinositol-anchored prion protein and Thy-1 differ in lipid composition. *J. Biol. Chem*. 279:7530-7536.

Burghardt, T. P., and N. L. Thompson. "Evanescent Intensity of a Focused Gaussian Light-Beam Undergoing Total Internal-Reflection in a Prism." Optical Engineering 23.1 (1984): 62-7.

Carnigli.Ck, L. Mandel, and K. H. Drexhage. "Absorption and Emission of Evanescent Photons." *Journal of the Optical Society of America* 62.4 (1972): 479-486.

Castellana, Edward T., and Paul S. Cremer. "Solid Supported Lipid Bilayers: From Biophysical Studies to Sensor Design." Surface Science Reports 61.10 (2006): 429-44.

Cordy, Joanna M., Hooper N. M., and Turner A. J., "The involvement of lipid rafts in Alzheimer's disease", *Molecular Membrane Biology (*2006) **23** (1) 111-122.

Dietrich, C., Bagatolli, L. A., Volovyk, Z. N., Thompson, N. L., Levi, M., Jacobson, K., et al. (2001). Lipid rafts reconstituted in model membranes. *Biophysical Journal, 80*(3), 1417-1428.

Griffiths, David J. Introduction to Electrodynamics. 3rd ed. Upper Saddle River, N.J.: Prentice Hall, 1999.

Kalb, E., Frey, S., & Tamm, L. K. (1992). Formation of Supported Planar Bilayers by Fusion of Vesicles to Supported Phospholipid Monolayers. *Biochimica Et Biophysica Acta, 1103*(2), 307-316.

Khan S, Pierce D, Vale RD (2000). Interactions of the chemotaxis signal protein CheY with bacterial Flagellar motors visualized by evanescent wave microscopy. *Curr Biol*,10:927-930.

Kiessling V, Crane JM, Tamm LK (2006). Transbilayer effects of raft-like lipid domains in asymmetric planar bilayers measured by single molecule tracking. *Biophys. J.* 91:3313-3326

Lee, C. S., & Bain, C. D. (2005). Raman spectra of planar supported lipid bilayers. *Biochimica Et Biophysica Acta-Biomembranes, 1711*(1), 59-71.

Lee, G. M., and K. Jacobson. "Lateral Mobility of Lipids in Membranes." Cell Lipids 40 (1994): 111-42.

Macdonald, R. C., Macdonald, R. I., Menco, B. P. M., Takeshita, K., Subbarao, N. K., & Hu, L. R. (1991). Small-Volume Extrusion Apparatus for Preparation of Large, Unilamellar Vesicles. *Biochimica Et Biophysica Acta, 1061*(2), 297-303.

Michel V & Bakovic M (2007). Lipid rafts in health and disease. *Biol. Cell* 99:129-140.

Rajendran, L. and Simons K. *(*2005). "Lipid rafts and membrane dynamics", *Journal of Cell Science* 118 (6) 1099-1102.

Sengupta, Prabuddha, Barbara Baird, and David Holowka. "Lipid Rafts, fluid/fluid Phase Separation, and their Relevance to Plasma Membrane Structure and Function." Seminars in cell & developmental biology 18.5 (2007): 583-90.

Simons K, Ikonen E (1997). Functional rafts in cell membranes. *Nature,* 387:569-572.

Simons, K., & Toomre, D. (2001). Lipid rafts and signal transduction (vol 1, pg 31, 2000). *Nature Reviews Molecular Cell Biology, 2*(3), 216-216.

Singer, S. J., & Nicolson, G. L. (1972). Fluid mosaic model of structure of cell-membranes. *Science, 175*(4023), 720.

Steyer JA, Almers W (1999). Tracking single secretory granules in live chromaffin cells by evanescent-feld fluorescence microscopy. *Biophys J*, 76:2262-2271.

Sund SE, Axelrod D (2000). Actin dynamics at the living cell submembrane imaged by total internal reflection fluorescence photobleaching. *Biophys J,* 79:1655-1669.

Tamm, L. K., and H. M. Mcconnell. "Supported Phospholipid-Bilayers." Biophysical journal 47.1 (1985): 105-13.

Veatch, S. L., and S. L. Keller. Organization in Lipid Membranes Containing Cholesterol. *Physical Review Letters* 89.26 (2002): 268101.

Veatch, S. L., & Keller, S. L. (2003). Separation of liquid phases in giant vesicles of ternary mixtures of phospholipids and cholesterol. *Biophysical Journal, 85*(5), 3074-3083.

Wang MD, Axelrod D (1994). Time-lapse total internal reflection fluorescence video of acetylcholine receptor cluster formation on myotubes. *Dev Dyn,* 201:29-40.

Weis RM, Balakrishnan K, Smith B, McConnell HM (1982). Stimulation of fluorescence in a small contact region between rat basophil leukemia cells and planar lipid membrane targets by coherent evanescent radiation. *J Biol Chem*; 257:6440-6445.